

PCCP

Accepted Manuscript



This is an *Accepted Manuscript*, which has been through the Royal Society of Chemistry peer review process and has been accepted for publication.

Accepted Manuscripts are published online shortly after acceptance, before technical editing, formatting and proof reading. Using this free service, authors can make their results available to the community, in citable form, before we publish the edited article. We will replace this *Accepted Manuscript* with the edited and formatted *Advance Article* as soon as it is available.

You can find more information about *Accepted Manuscripts* in the [Information for Authors](#).

Please note that technical editing may introduce minor changes to the text and/or graphics, which may alter content. The journal's standard [Terms & Conditions](#) and the [Ethical guidelines](#) still apply. In no event shall the Royal Society of Chemistry be held responsible for any errors or omissions in this *Accepted Manuscript* or any consequences arising from the use of any information it contains.



Journal Name

ARTICLE

From Linear to Cyclic Oligoparaphenylenes: Electronic and Molecular Changes Traced in the Vibrational Raman Spectra and Reformulation of the Bond Length Alternation Pattern

Received 00th January 20xx,
Accepted 00th January 20xx

DOI: 10.1039/x0xx00000x

www.rsc.org/

Miriam Peña Alvarez,^{a,b} Lili Qiu,^b Mercedes Taravillo,^a Valentín G. Baonza,^a M Carmen Ruiz Delgado,^c Shigeru Yamago,^d Ramesh Jasti,^e Juan T. López Navarrete,^c Juan Casado,^{*c} Miklos Kertesz^{*b}

Cyclic paraphenylenes, [n]CPP, and linear paraphenylenes, [n]LPPs, formed by n benzenes, are investigated by Raman spectroscopy for $n=5$ to 12 and density functional theory (DFT) for $n=4$ to 20. The information on the experimental Raman frequencies and intensities, combined with the DFT computations and reported X-ray diffraction structures, provides a consistent interpretation of the Raman spectra and allows to establish relevant structure-property trends. Structural and electronic effects such as benzene ring bending, inter-ring torsions, π -conjugation (aromaticity) and orbital energy gaps as a function of the linear elongation in [n]LPP versus macrocyclic curvature in [n]CPP and of the molecular size (i.e., polymer limit) are systematically analyzed on the basis of the vibrational Raman properties. Changes in the BLA as an indicator of the degree of quinonoid character are analyzed and linked to the Effective Conjugation Coordinate (ECC) model. The BLA patterns involved in twisted and non-twisted conformations and in different species (bipolarons, quinonoid tautomers, and the ECC active modes) are compared and their differences are discussed. This paper offers a unified interpretation of structural and electronic aspects related with the evolution from linear 1D π -systems to cyclic 2D structures.

Introduction

Cyclic [n]paraphenylenes ([n]CPPs, Fig.1) are closed macrocyclic molecules formed by n benzene units in a fashion that could be considered as the shortest slice of an armchair carbon nanotube (CNT).¹⁻¹³ [n]CPPs are capable of encapsulating guest molecules,¹⁴ their electronic properties are size-tunable^{14,15,16} and markedly differ from those of CNTs.¹⁷ They furthermore provide a link between small oligomers and polymers of phenylenes. Various [n]CPPs have been characterized by X-ray diffraction (XRD), vibrational and electronic spectroscopy and electrochemistry.^{4-5,18,19,20,21,22,23} Computational modeling based on density functional theory has been also used to interpret the experimental data.¹² An important underlying question in all these studies concerns the structural and electronic features that make [n]CPPs singularly different to linear [n]paraphenylenes ([n]LPPs, Fig.2). It is well

known that linear π -conjugation shapes the structure of [n]LPPs in competition with ring aromaticity. One therefore wonders if in [n]CPPs a similar cyclic π -conjugation effect exists and which are its structural and spectroscopic marks. In chemical terms, the issue of π -conjugation has been addressed by the degree of aromatic (A) vs. quinonoid (Q) structural character.^{2,4,24,25} A and Q are illustrated in Fig. 1 for [6]CPP (for the same A the twisted and non-twisted versions are also shown). For instance, Bachrach and Stück showed by using DFT at the B3LYP/6-31G(d)²⁶ level that Q structure, called “bond-shift”, can be found as a local metastable minimum on the potential energy surface (PES) for $n=3, 4, 5$ and 6.



Figure 1. Schematics of structural isomers of [6]CPP: a) Aromatic D_{3d} , twisted conformation; b) Aromatic D_{6h} , non-twisted conformation; c) Quinonoid D_{6h} , non-twisted conformation.



Figure 2. Structural isomers of [3]LPP. a) Aromatic C_{2v} , twisted conformation; b) Aromatic D_{2h} , non-twisted conformation; c) Diradical Aromatic C_{2v} , non-twisted conformation; and Quinonoid D_{2h} non-twisted conformation.

^aMALTA-Consolider Team, Department of Physical Chemistry, Chemistry faculty, University Complutense of Madrid, 28040 Madrid, Spain.

^bDepartment of Chemistry and Institute of Soft Matter, Georgetown University, 37th and O Streets, NW, Washington, D.C. 20057-1227, USA.

^cDepartment of Physical Chemistry, University of Málaga, CEI Andalucía Tech, Campus de Teatinos s/n, 29071-Málaga, Spain. Fax: 0034952132000

^dChemical Research, Kyoto University, Uji 611-0011, Japan

^eDepartment of Chemistry and Biochemistry and Materials Science Institute 1253, University of Oregon, Eugene, Oregon 97403, USA

Electronic Supplementary Information (ESI) available: [details of any supplementary information available should be included here].

In this scenario, [n]LPPs will aid the interpretation of the properties of their cyclic cousins.^{27,28} The alternative A (twisted and non-twisted) and Q structures for [n]LPP are also illustrated in Fig.2.

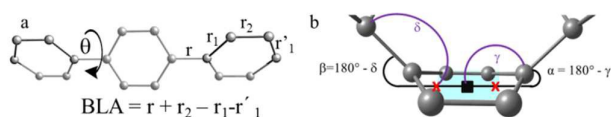
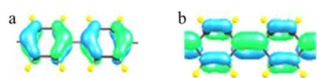


Figure 3. a) Torsional angle (θ) between two neighboring benzene units; and the CC bond distances (r , r_1 and r_2). b) Out-of-plane bending angles α and β are defined as $\alpha = 180^\circ - \gamma$; $\beta = 180^\circ - \delta$. Different centroids are indicated by X and ■ and are used to calculate the out-of-plane deformation of the benzene units. For [n]LPPs, $\alpha = \beta = 180^\circ$.

A way to quantify the aromatic/conjugation or A/Q interconversion deals with the bond length alternation (BLA) pattern which involves rather different deformations on linear and cyclic cases, one along the [n]CPP perimeter and another along the linear [n]LPP chain. In fact this paper shows some of these differences in the BLA patterns for the two series. However, generally in the literature, any A to Q change has been quantitatively described by the same BLA parameter²⁹ using the following formula and the definitions in Fig. 3:

$$BLA = r + r_2 - r_1 - r_1' = r + r_2 - 2r_1 \quad (1)$$

when the inter-ring bond (r) is long, and r_1 and r_2 are close in value, the structure is aromatic with $BLA > 0$. For [n]CPPs $r_1 = r_1'$. When r is short, and $r_1 > r_2$ then $BLA < 0$ and the structure is quinonoid.



Scheme 1. Orbital pattern for the HOMO (a) and LUMO (b) of a section of an oligoparaphenylenes. H atoms are in yellow.

The different orbital patterns of the relevant HOMO and LUMO frontier molecular orbitals in Scheme 1 are the fundamental reasons why the BLA changes significantly in the A \rightarrow Q direction when the occupancy between HOMO and LUMO is switched. For this reason the HOMO-LUMO bandgap strongly depends on the degree of BLA as shown in the literature.^{29,35} As a consequence, the strong vibronic coupling between some A_g -like symmetry vibrations (mimicking a BLA stretching modes) and the HOMO-LUMO gap is responsible for the main bands of the Raman spectra which are thus associated with vibrational coordinates that involves a certain degree of BLA distortion. In other words, due to this strong coupling of the BLA-like deformation and the gap, the Raman intensities and frequencies are spectroscopic markers of the BLA changes, a connection that is emphasized in the Effective Conjugation Coordinate (ECC) theory.^{29,30,31}

The ECC theory defines a totally symmetric stretching vibration corresponding to the in-phase shrinking/stretching of the C-C/C=C consecutive bonds (ECC mode) in such a way that their vibrational amplitudes match the A \leftrightarrow Q geometrical transformation, or BLA deformation.^{31, 32, 33} Since the ECC mode is not a vibrational eigenfunction, its intensity appears distributed among the few symmetric C-C/C=C stretching

normal modes of the vibrational Raman spectrum (ECC-like bands). The frequency and intensity behavior of these ECC-like bands give insights of the BLA alteration in the A/Q context: for example, a ECC band frequency downshift is related with the variation of the BLA value towards zero (to the transition from A to Q or vice versa).^{31,32}

Here we focus on the [n]-dependence of BLA for both [n]CPP and [n]LPP series together for the first time in connection with linear and cyclic π conjugations and with the A \leftrightarrow Q transformation.^{33,34} Additional open questions we attempt here to solve are:

1. Is this quinonoidization effect in [n]CPP a result of a valence tautomerization, i.e., are there two different local minima on the electronic ground state PES?³⁵
2. The ground state structures of highly doped [n]LPPs and poly-p-phenylene (PPP) are generally understood to have bipolarons, which have a structure containing quinonoid characteristics, as expressed by a negative BLA. Is this kind of quinonoidization similar to that argued in [n]CPPs?
3. It has been shown that the strong Raman A_{1g} vibrations of [n]LPPs present a large BLA component. Do the main Raman bands of [n]CPPs also involve a strong BLA component?

To address these points, we obtain and compare the geometries of the [n]CPP and [n]LPP as a function of n paying attention to the distinctive electronic effects (i.e., hybridization, electronic delocalization due to the loss of local planarity in Fig. 3b etc.) in both series in order to highlight differences between linear and cyclic π -conjugation. The discussion is particularly important in the limit of highly strained [n]CPPs (those with smaller n values). Then we address the main features of the Raman spectra, and the connections of the Raman active modes to the BLA pattern and to the A/Q interplay. A unified vision of linear versus cyclic π -conjugation is in the conclusions section. Along the paper, when possible, computed structures are compared with available XRD data. Furthermore, we also present new experimental data on the Raman spectra for [5]CPP.

Methods

[n]CPP with $n = 7, 8, 9, 10, 11$ and 12 were synthesized by using a synthetic strategy through multinuclear arylplatinum complexes,³⁶ while [5]CPP and [6]CPP were synthesized through Suzuki-Miyaura cross-coupling.^{4,5} For comparison of the cyclic and linear oligomers, we recorded the Raman spectra of [5] and [6]LPP (samples were purchased from TCI and studied without further purification).

All reported energy values and geometrical parameters refer to the geometry-optimized structures using the B3LYP/6-31G(d,p) method. We have also carried out DFT calculation with an extended basis set B3LYP/6-311+G(2df,p), and with two further functionals with dispersion content (wB97xD and B3LYP-D3/6-31G(d,p)). These latter two provided essentially the same results as B3LYP/6-31G(d,p) which was therefore chosen in all presented computations as a good compromise between computational cost and accuracy. Validation data are provided in Tables S1-S3.

Unless noted otherwise, all geometries were optimized without constraints, and all minima were confirmed by vibrational calculations with all frequencies being real. The exceptions are: planar [n]LPPs and non-twisted [n]CPPs, which were optimized by keeping the D_{2h} and D_{nh} symmetry, respectively. Raman frequencies have been scaled: the factor 0.97 was used for the 450-900 cm^{-1} region and 0.9675 for the region between 1100-1700 cm^{-1} . The assignments of the bands refer to normal modes and symmetry labels of the respective high symmetry conformation, D_{nh} . Vibrational Raman intensity for a given j -th vibrational normal mode, in the non-resonant approximation, is proportional to I_j as given by:³²

$$I_j = 45\alpha'^2 + 7\gamma'^2 \quad (2)$$

where α'^2 and γ'^2 are the derivatives with respect to the j -th normal mode displacements of the trace and anisotropy of the polarizability term, respectively.

Table 1. XRD reported for [n]CPPs and [n]LPPs used.

$n=$	5	6	7	8	9	10	12	[3]LPP	[4]LPP
Ref. code ^a	HIYLIM	LAXKOM	RIRYEV	QEBKAL	VAMWOX	QEBKEP	ONIZIV	TERPHE15	QUPHEN
Ref.	4	5	18	19	20	21,22	23	37	38, 39
R-%	4.86	5.06	6.48	4.14	9.52	5.05	9.04	3.2	4.5

^aCambridge Structural Database (CSD).

Raman measurements at room conditions of the different [n]CPP were conducted with an Invia Reflex Raman RENISHAW microscope with a 785 nm excitation wavelength, with a spectral resolution of 0.5 – 1 cm^{-1} . A Senterra dispersive micro Raman spectrometer from Bruker with a 785 nm excitation wavelength was used for the characterization of [5]CPP and [5]-[6]LPP at room temperature with a standard spectral resolution of 3 cm^{-1} . [5]CPP was measured under an inert atmosphere. Experimental intensities are quoted as their heights when fitted with Lorentzian profiles with FWHM ranging between 6 and 15 cm^{-1} , depending on the band, but constant for each band regardless of n . Crystal structures have been taken from the CSD database, see Table 1. The XRD data for [11]CPP²⁵ were not used because of spurious H atoms in the structure. Similarly the structures for [9]CPP and [12]CPP were not used in our comparisons due to their large R-factors.

We have calculated by B3LYP/6-31G(d,p) the non-resonant Raman spectra of the [n]CPPs. The most intense bands are the A_{1g} modes for molecules with D_{nh} or $D_{n/2,d}$ symmetry while for molecules with lower symmetries we will refer them as A_{1g} -like normal modes.

The normal mode displacement vectors, \vec{L}_j , can be decomposed into modes expressed in internal coordinates, \vec{B}_k \vec{B}_k :

$$\vec{L}_j = c_{j,1}\vec{B}_1 + \sum_{k>1} c_{j,k}\vec{B}_k \quad (3)$$

Here mode $k=1$ corresponds to that special BLA mode, denoted as \vec{B}_1 , which carries most of the Raman intensities according to the ECC model and this mode has been called the amplitude mode (AM) or \mathcal{A} - or ECC mode.^{31,32,40} $c_{j,1}$ is the coefficient of the B_1 component of the j -th normal mode. Vector \vec{B}_1 is a displacement vector with A_{1g} (or approximate A_{1g}) symmetry. In these conditions, vibrational Raman intensity theory describes the non-resonant Raman intensity of the j -th A_{1g}

mode, coupled with the \vec{B}_1 one, as approximately proportional to the square of that component's coefficient:

$$I_j = |c_{j,1}|^2 \quad (4)$$

The ECC model has been used to obtain insights into the dominant A_{1g} Raman modes for a variety of conjugated systems even though the specific nature of the special \vec{B}_1 mode is rather unknown.^{31,32,33} It is clear however that this BLA mode is fully delocalized over the complete sequence of C-C/C=C bonds which represents a normalized displacement that is proportional to a sum over all repeat units of the following displacement vectors, for notation of Fig. 3a:

$$\vec{B}_{BLA} = \sum (\delta r_1 + \delta r_2 - \delta r_1' - \delta r_1'') \quad (1a)$$

This mode is referred to as the $k=1$ mode, \vec{B}_1 , in eq. (3). Based on eqs. (3) and (4), we can estimate the displacements of this special AM or ECC mode from the sum of the product between the square root of the intensity of the A_{1g} modes and the respective displacement vectors:

$$\vec{B}_1 = c_1 \sum_{i \in A_{1g}} \pm I_i^{1/2} \vec{L}_i \quad (5)$$

where c_1 is the normalization factor and the sign of each term is chosen to ensure that all contributions are in phase.

Results

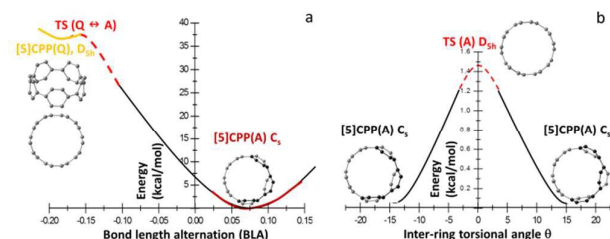
I. Energies and topology of the PES

I.1. Aromatic-Quinonoid transition. [n]CPPs have received much attention in this regard, since with decreasing size and increasing strain, the benzene rings become deformed and benzene aromaticity along the bonds designated as r_1 in Fig. 3 is inhibited due to an increasing sp^3 character which provokes a certain degree of quinonoid character in the rings.

Scheme 2a shows the general shape of the potential energy curve for the small [n]CPPs ($n=4$, and 5) between the quinonoid and the aromatic local minima as a function of the bond length alternation (BLA) coordinate. The respective numerical values are summarized in Table 2. For instance, the BLA of the [5]CPP from its quinonoid (Q) to its aromatic conformation (A) varies from -0.185 Å to 0.064 Å. This change is accompanied by significant changes in the bending angles indicating a significant loss of benzene aromaticity leading to highly localized exo-double bonds in the quinonoid configuration, explaining its higher energy compared to the aromatic form.

The transition state (TS) for [4]CPP connecting the quinonoid local minimum and the aromatic absolute minimum of the PES was located by Bachrach and Stück.²⁶ In [5]CPP through a rigid scan (where the CC distances are modified along a linear grid connecting the A and Q structures without relaxation⁴¹), we find a tentative non-twisted TS with an energy barrier from A to Q of about 39 kcal/mol. The real TS obtained by relaxation should give an even lower energy barrier but we were unable to obtain the exact structure of this TS even though both minima are characterized by 3N-6 real vibrational frequencies. However, we are not able to find a quinonoid tautomer for any [n]CPP with $n>5$. This suggests that [5]CPP is the limiting size for the existence of the quinonoid structure as a valence tautomer. Table 2 summarizes our calculated A/Q parameters

for the structures for $n=4, 5$, and 6. The geometries and energies behave as expected. The $E(Q) - E(A)$ difference increases with increasing size. Larger degree of bending of the benzene units in the smaller [n]CPPs appears with a concomitant larger pyramidalization of all carbons.²⁶ It appears that it is this pyramidalization that assists the development of the inter-ring double bonds and makes the quinonoid structure energetically competitive, but only for very small [n]CPPs.



Scheme 2. a) Schematic potential energy curves for [5]CPP; TS: transition state. b) Schematic of the potential energy curve for [5]CPP indicating the conformational pathway between two degenerate structures through its non-twisted D_{5h} structure.

1.2. Twisted to non-twisted aromatic transition. Now we focus on the barriers between the two energetically competitive aromatic structures, the low (twisted, $D_{n/2,d}$) and high (non-twisted, D_{nh}) symmetry conformations in Scheme 2b which further illustrates the barrier between them. The per-ring energy difference [kcal/(mol·ring)] between these is shown in Fig. 4a as a function of n . For both [n]CPP and [n]LPP series, these energy differences increase with the increasing size towards a common value around 1.6 kcal/(mol·ring). Furthermore these differences are larger in [n]LPPs, for instance [4]LPP requires about +1.3 kcal/(mol·ring) for planarization, while only about +0.2 kcal/(mol·ring) in [4]CPP due to the strong bending in the smaller [n]CPPs.²⁴ The numerical values are provided in Tables S4 and S5.

Table 2. Energy differences between the quinonoid local minimum (Q) and aromatic minimum (A), barriers and selected structural data for [n]CPPs. EB is the energy barrier relative to $E(Q)$; energies are in kcal/mol, distances are in Å, angles are in degrees.

n	Sym. (Q)	Sym. (A)	$E_Q - E_A$	E_B	BLA for						
					A BLA	Q BLA	TS (A↔Q)	αA	αQ	βA	βQ
4	D_{4h}	D_{2d}	10.4	9.9	0.074	-0.222	-0.105	20	29	25	16
5	D_{5h}	C_s	37.5	0.7	0.064	-0.185	-0.153	16	22	20	13
6	-	D_{3d}	-	-	0.062	-	-	14	-	16	-

Since the non-twisted D_{nh} structures are unstable, they are characterized by imaginary frequencies which are shown in Fig. S1a and Fig. S1b as a function of n . Interestingly, they follow a pattern as a function of size depending on whether the molecule is cyclic or linear. For even [n]CPP, there are $((n/2)-1)$ different ways the structure can deviate from a non-twisted geometry, and for odd [n]CPPs there are $((n-1)/2)$ (degeneracies are observed). The lowest energy displacement corresponds to the largest imaginary frequency and it corresponds to an alternating in-out displacement which represents the largest possible

avoidance of H...H non-bonded repulsions. This is significant because it means that there are $((n/2)-1)$ different conformers for the even [n]CPPs and $((n-1)/2)$ for the odd [n]CPPs.

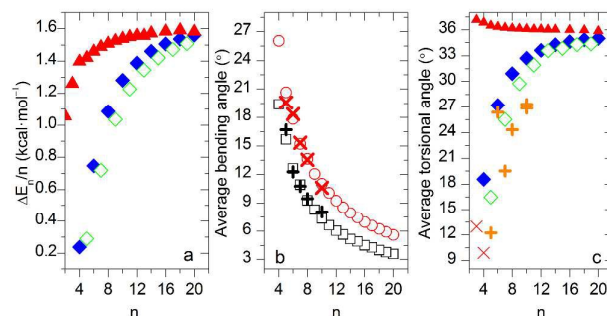


Figure 4. B3LYP/6-31G(d,p) data: a) Energy difference per phenyl unit between the twisted and non-twisted conformations, $\Delta E/n$, as a function of n . \blacklozenge and \blacklozenge represent the even and odd CPPs, respectively, while \blacktriangle is for [n]LPPs. b) Computed average bending angles as a function of n : \square and \circ for α and β respectively; $+$ and \times are for XRD data. ^{45,18,19,21,22,23} c) Torsional angles between neighboring benzenes, \blacktriangle for LPPs, \blacklozenge and \blacklozenge correspond to even and odd [n]CPPs, respectively. $+$ refers to XRD data for [n]CPPs ^{45,18,20,21,22,23} and \times for [n]LPPs. ^{37,38,39}

II. Geometrical and electronic parameters

II.1. Bending and Torsions. While in [n]LPPs the benzene rings remain planar, in [n]CPPs they are bent.^{11,12} In Fig. 4b we have plotted the experimental and theoretical bending angles of [n]CPPs, as defined in Fig. 3b, as a function of n . In agreement with results previously reported in the literature,^{12,26} out of plane six member ring deformations grow dramatically when the [n]CPP becomes smaller. Fig. 4c shows the computed interring torsional angles of [n]LPP and [n]CPP. Even and odd [n]CPPs follow an alternating pattern of \pm torsions, however this undulating distribution of torsions in odd [n]CPPs is not uniform (Fig. 4c thus shows average torsional values). The [n]LPPs have torsional angles that are slightly higher for smaller n and they trend towards a constant value, around 36°, for the larger n values.⁴² Our data are in agreement with those of Chen *et al.*⁹

II.2. Computed bond length alternation. In Fig. 5a and Fig. 5d we have represented the BLA dependence on n for both [n]CPPs and [n]LPPs obtained from our optimized structures and from literature XRD data. In the case of the [n]CPPs, the agreement between theory and experiment is excellent. There are only few experimental data reported in the literature for [n]LPPs which precludes an extensive analysis. The comparison of the BLAs between [n]LPP and [n]CPP shows that both systems have very similar values for $n > 8$, in line with the decreasing bending of the benzene rings. BLAs behave very similarly in the twisted and non-twisted [n]CPPs and none of these show any significant quinonoid character. The BLA values for the non-twisted conformers are slightly smaller compared to the twisted analogues in line with some gain of aromatic character in the latter.

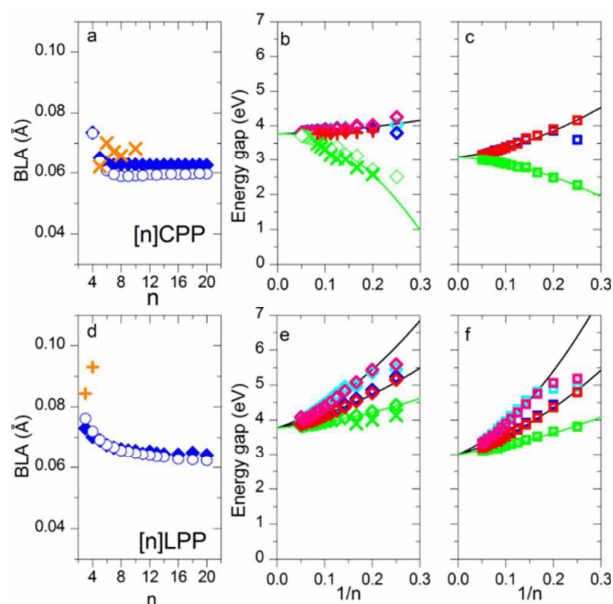


Figure 5. Bond length alternation as a function of n : a) [n]CPP; d) [n]LPP. \circ and \diamond stand for B3LYP/6-31G(d,p) non-twisted and twisted conformational data, respectively; \times and $+$ stand for [n]CPP and [n]LPP XRD data. $4.5^{18,20,21,22,23,37,38,39}$ Energy gaps, versus $1/n$ for: b) Twisted [n]CPPs, c) Non-twisted [n]CPPs, e) Twisted [n]LPPs, f) Non-twisted [n]LPPs. \diamond corresponds to twisted and \square to non-twisted conformations. Green symbols for HOMO-LUMO values, red symbols for HOMO-LUMO+1 and HOMO-1 \rightarrow LUMO and blue symbols for the HOMO \rightarrow LUMO+2 and HOMO-2 \rightarrow LUMO. \times and $+$ for experimentally assigned HOMO-LUMO and the HOMO-LUMO+1 bands for [n]CPP respectively. $4,5^{18,20,21,22,23}$ \times for experimentally assigned HOMO-LUMO bands in [n]LPP.⁴³

III.3. BLA and energy gaps. There is a striking difference between the energy gaps as a function of n for [n]LPPs and [n]CPPs in Fig. 5. The higher bending and lower torsion in [n]CPPs have a concomitant impact on the HOMO-LUMO gaps⁴⁴ which clearly decrease with increasing size in [n]LPP.⁴⁴ However, the HOMO-LUMO gap behavior on the [n]CPPs becomes one of the most distinctive features regarding [n]LPPs because it is narrowed with the decreasing size. The energy gap data, fitted to a second order polynomials in n^{-1} , converge to a common limiting value of 3.77 eV for twisted, and around 3.05 eV for non-twisted [n]CPPs as $n \rightarrow \infty$. In this limit, non-twisted [n]CPPs and [n]LPPs converge to the same value in concert with the idea that they approach the edges of the bands of the respective infinite chains (the energy gap of PPP is around these limits, at 3.4 eV).^{45,46}

This discussion on the structural and electronic features of [n]CPPs establishes their distinctive behavior compared to the [n]LPPs especially for smaller n (see Fig. S2). Further insights into this comparison are obtained in next sections by the analysis of the BLA in terms of Raman shifts and intensities, and the discussion of the ECC model as it relates to the A/Q transformation and Raman data.

III. Vibrational Spectra and Structures

In this section we discuss those aspects of the Raman spectra concerning the most intense bands with A_{1g} (A_{1g} -like)

symmetry on the basis of the DFT computations. Table 3 summarizes our assignments for [6]CPP and [6]LPP.

Table 3. Experimental and theoretical wavenumbers (in cm^{-1}) for [6]CPP and [6]LPP, species of symmetry (non-twisted D_{nh} conformation) and the vibrational assignment in terms of internal coordinates.

[6]CPP			[6]LPP			
Exp.	Theor.	Sym.	Vibrational description	Exp.	Theor.	Sym.
504	499	A_{1g}	RFM	--	--	--
	770	A_{1g}	$\beta(\text{CC}) + \beta_{\text{antisym}}(\text{phenyl}) +$	--	--	--
	784	A_{1g}	RFM (for CPPs) + $\beta(\text{C-H})$	--	--	--
804	804	A_{1g}		770	772	A_g
1192	1179	E_{2g}	$\beta(\text{phenyl}) + \nu(\text{C-C}) + \omega(\text{CH})$	--	--	--
1200	1185	A_{1g}	$\beta(\text{C-H}) + \nu(\text{C-C})_{\text{interring}}$	1219	1222	A_g
1252	1244	E_{2g}	$\beta(\text{phenyl}) + \nu(\text{C-C})_{\text{interring}} + \beta(\text{C-H})$	1269	1263	A_g
1263	1245	A_{1g}	$\beta(\text{phenyl}) + \nu(\text{C-C})_{\text{interring}} + \beta(\text{C-H})$	1278	1278	A_g
1269	1264	E_{1g}	$\nu(\text{C-C}) + \omega(\text{CH}) + \beta(\text{phenyl})$	--	--	--
1504	1496	E_{2g}	$\nu(\text{C}_{\text{ipso}}\text{-C}_{\text{ortho}})$	1486	1485	A_g
1567	1576	A_{1g}	$G_{A_{1g}}: \nu(\text{C-C})_{\text{transversal}}$	1593	1594	A_g
1584	1592	E_{2g}	$G_{E_{2g}}: \nu(\text{C-C})_{\text{trans}} + \nu(\text{C-C})_{\text{long}}$	--	--	--

RFM: radial flexural mode or $\text{C}_{\text{ipso}}\text{-C}_{\text{ipso}}$ bond vibration with motion outward relative to the center of the macrocycle and the $\text{C}_{\text{ortho}}\text{-C}_{\text{ortho}}$ bond motion inward; **$\beta(\text{C-C})$:** C-C bond bending mode; **$\beta_{\text{antisym}}(\text{phenyl})$:** antisymmetric phenyl breathing mode, $\text{C}_{\text{ortho}}\text{-C}_{\text{ortho}}$ with motion inward relative to the benzene center, C_{ipso} outward. **$\beta(\text{phenyl})$:** symmetric phenyl breathing mode; **$\omega(\text{CH})$:** C-H wagging mode; **$\nu(\text{C-C})_{\text{interring}}$:** C-C inter-ring stretching mode; **$\beta(\text{C-H})$:** C-H bending mode; **$\nu(\text{C}_{\text{ipso}}\text{-C}_{\text{ortho}})$:** $\text{C}_{\text{ipso}}\text{-C}_{\text{ortho}}$ inter-ring stretching mode; **$\nu(\text{C-C})_{\text{transversal}}$:** C-C stretching mode along the transversal direction of the macrocycle; **$\nu(\text{C-C})_{\text{long}}$:** C-C stretching mode along the longitudinal direction of the ring.

According to the ECC model, these bands show significant intensities because their displacements contain a large component from the ECC mode as described by eq. (3). In general the non-twisted [n]CPP structures give rise to simpler spectra, thus we first describe their strongest Raman bands and extrapolate the assignments to the twisted (i.e., lower symmetry) homologues on the basis of the very close similarity among the respective normal modes.

III.1 The 450 cm^{-1} and 900 cm^{-1} low frequency region. In Fig. 6 and Table 3 we gathered the experimental and computational results for [6]CPP and [6]LPP between 450 cm^{-1} and 900 cm^{-1} , while Figs. S3 to S7 show the experimental and theoretical spectra of [n]CPP and [n]LPP from $n=4$ to 20.

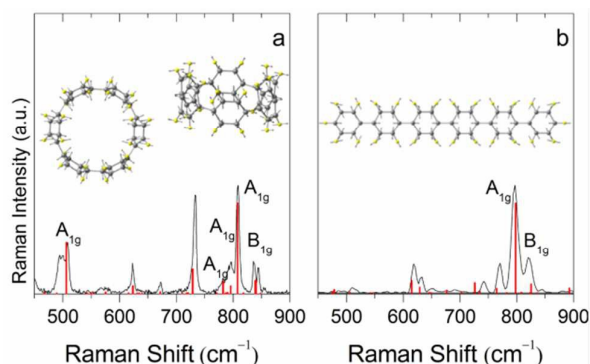


Figure 6. Raman spectra (black lines) in the region 450 – 900 cm^{-1} of a) [6]CPP and b) [6]LPP. Red vertical bars are the B3LYP/6-31G(d,p) calculated spectra for D_{3d} [6]CPP and non-twisted D_{2h} [6]LPP. Theoretical frequencies are scaled by a factor of 0.97. Inserts show the displacement vectors of the strongest A_{1g} bands. a) left RFM mode. a) right C_{ipso} - C_{ortho} - C_{ipso} bending mode.

The spectrum of [6]CPP presents four major A_{1g} bands, one around 500 cm^{-1} and other three around 800 cm^{-1} . [6]LPP however has only one strong A_{1g} band around 800 cm^{-1} (similar differences occur for all n in Figs. S3–S7). The 500 cm^{-1} band is due to a breathing-type motion of the CPP ring as a whole where the C_{ipso} - C_{ipso} bonds move outward relative to the center while the C_{ortho} - C_{ortho} bonds move inward, thus resulting in a vibration along the [n]CPP perimeter, to which we will refer as radial flexing mode or RFM.^{8,9} In the linear paraphenylenes the parent mode has B_{2u} symmetry and is not Raman active. The three 750 - 850 cm^{-1} bands in twisted [n]CPPs correspond to three A_{1g} modes arising from C_{ipso} - C_{ortho} - C_{ipso} bending modes coupled with antisymmetric phenyl breathing modes and with the RFM mode. The computed frequencies of these A_{1g} bands show an upshift of 20 cm^{-1} from $n=4$ to $n=9$ for the twisted conformers. This shift is 35 cm^{-1} for the non-twisted conformations, as shown in Figs. S6–S7.

III. 2 The 1100-1300 cm^{-1} region. Fig. 7 shows the experimental spectra in the 1100 - 1300 cm^{-1} region for [6]CPP (see Figs. S8 - S11 for the experimental and theoretical spectra for the rest of compounds).

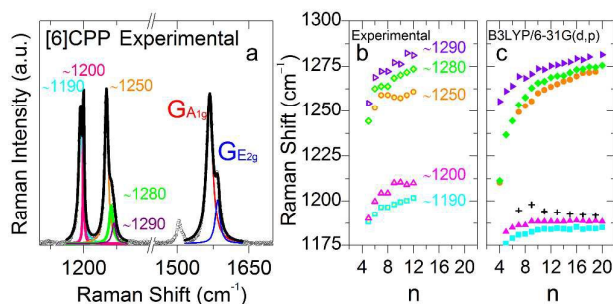


Figure 7. a) Raman spectrum (black lines) of [6]CPPs in the 1100 - 1700 cm^{-1} region. The band deconvolutions are shown in color. Raman frequencies evolution of the main bands in the 1175-1300 cm^{-1} region. b) Experimental data. c) Calculated for twisted [n]CPPs; Theoretical frequencies are scaled by 0.9675.

In the 1200 cm^{-1} region two main A_{1g} bands dominate the spectrum with the assignment given in Table 3. These are correlated with the bands at 1220 cm^{-1} and 1280 cm^{-1} of [n]LPPs.^{24,34,42,47} A discussion of the non- A_{1g} modes is given in the ESI file. In regard of these two A_{1g} Raman bands, their intensity ratio ($I_{1280A_{1g}}/I_{1220A_{1g}}$) has been correlated with the domain-size of linear π -conjugation in [n]LPPs and torsional angles (see Figs. S12-S15).^{33,42} In next section we discuss the behavior of this ratio for linear versus cyclic PPs in the context of the ECC theory.

III.3 The BLA modes in the 1500 - 1600 cm^{-1} region. The most intense Raman bands of the spectra appear in this range and are shown in Fig. 7. The displacements associated with these bands contain a large component of the totally symmetric BLA mode similar to the [n]LPPs.^{30,31} A prominent feature around 1600 cm^{-1} with two components at lower and higher frequencies, denoted as $G_{A_{1g}}$ and $G_{E_{2g}}$, stands out in this region. The G terminology refers to the C-C stretching band characteristic of graphitic materials and CNTs.^{8,9,24} The most intense of these two components comes from an A_{1g} mode related to the collective C-C stretching mode that follows the BLA pattern, while the shoulder at higher frequencies is an E_{2g} mode also related to C-C stretches.²⁴ A weak band around 1500 cm^{-1} assigned to the C_{ipso} - C_{ortho} stretching mode, referred hereafter as G_{io} , is observed (of E_{2g} and E_2 symmetry for even and odd n respectively, see Figs. S16-S17).^{8,9} Given that this $G_{A_{1g}}$ band is the most intense of the spectra, its intensity and Raman shift are of particular importance for π -conjugation in the context of the ECC model.^{48,30,31,32,49}

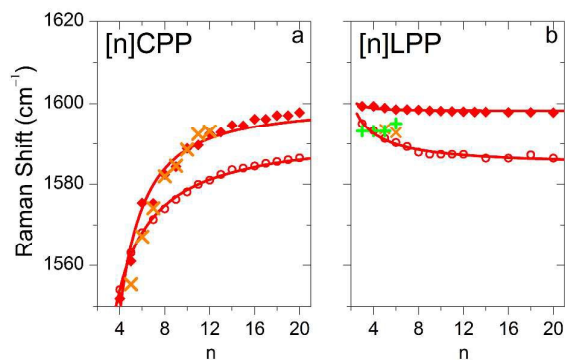


Figure 8. $G_{A_{1g}}$ band Raman shift vs n for: a) [n]CPPs, b) [n]LPPs. \circ for non-twisted computed data and \blacklozenge for twisted. \times for [n]CPP experiments. $+$ for [n]LPPs experiments.⁵⁰ Lines are provided to guide the eye.

In Fig. 8 we show the $G_{A_{1g}}$ frequencies as a function of n from which we deduce the following:

- For twisted [n]LPPs, the $G_{A_{1g}}$ mode slightly downshifts with increasing n while this change is more pronounced for the non-twisted conformers of [n]LPPs.
- In the [n]LPPs and [n]CPPs series, the $G_{A_{1g}}$ Raman bands are always at higher frequency values for the twisted than for the non-twisted conformers.
- For both [n]LPPs and [n]CPPs series, the frequency of the $G_{A_{1g}}$ bands converge to similar values in the polymeric

limit^{33, 51} ($n \rightarrow \infty$) in accordance with the reduction of the curvature which unifies the linear and cyclic behaviors.

iv) It is well known that in [n]LPPs the electron confinement of electron density by aromaticity in the phenyl rings precludes extensive inter-ring π conjugation, and so small Raman shift variations are observed from molecule to molecule.⁴³ In concordance with this Raman shift – π -conjugation relationship, the Raman frequencies of the non-twisted [n]LPPs are more downshifted with respect their twisted counterparts.

v) Both in the twisted and non-twisted models of the [n]CPP series these $G_{A_{1g}}$ bands show a much larger frequency variation as a function of n compared to [n]LPP. This large frequency dispersion is attributed to the strong bending of the benzene rings which breaks down its aromaticity and allows larger π -conjugation for [n]CPP, especially for smaller n .²⁴ (Fig. 5). It can also be attributed to the absence of terminal constraints in [n]CPP.

vi) Interestingly, the sign of the dispersion shifts with increasing size in [n]CPP and [n]LPP are opposite. In [n]LPPs it is known that when adding more phenyl units to the chain the conjugation is increased, so it explains why the $G_{A_{1g}}$ downshifts with the increasing n .⁴³ On the other hand, in [n]CPPs the increasing strain on the smaller units leads to considerably lower torsions which favor the conjugation between phenyl units developing through-space orbital interactions.⁵² Thus this explains the opposite trends in the shifts between [n]CPPs and [n]LPPs.

III. 4 Size dependence of the intensities of selected A_{1g} modes. We now address the intensity evolution of the A_{1g} bands as a function of n in Fig. 9.

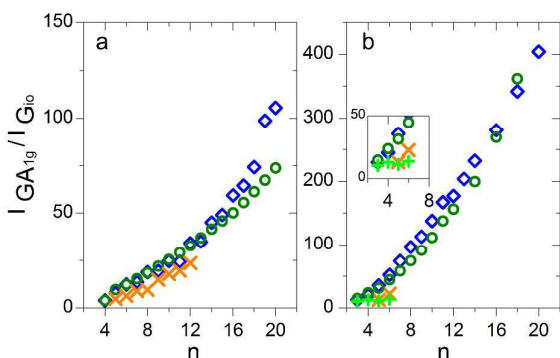


Figure 9. Relative Raman Intensities of the $G_{A_{1g}}$ band as a function of n compared to the respective G_{i_o} band intensity. a) [n]CPPs; b) [n]LPPs. \circ for B3LYP/6-31G(d,p) non-twisted conformations, \diamond for B3LYP/6-31G(d,p) twisted ones and \times for experiments. $+$ for experimental data for [3]LPP to [6]LPP.⁵⁰

The calculated non-resonant Raman intensities were plotted relative to that of the G_{i_o} band, as its intensity keeps almost unaltered with the molecular size (Fig. S17 shows the experimental Raman spectra normalized to their G_{i_o} bands). The first observation is that this relative intensity of the $G_{A_{1g}}$ band increases superlinearly with increasing n . The

experimental $I(G_{A_{1g}})/I(G_{i_o})$ intensity ratios are in satisfactory agreement with computations.

Fig. 10 shows the intensity ratio between the two A_{1g} bands at 1200 cm^{-1} and at 1280 cm^{-1} relative to the $G_{A_{1g}}$ band in both [n]CPPs and [n]LPPs. For larger n , as the ring strain is reduced, and therefore these intensity ratios in the two series converge to a similar value. For smaller n the significantly different intensity ratios represent another manifestation of the particular electronic structure promoted by ring bending and dearomatization.⁴³

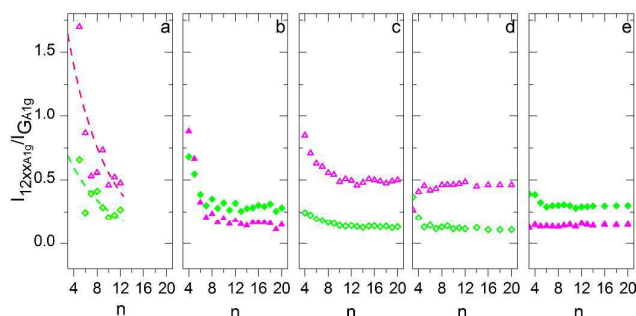


Figure 10. $I_{1200 \times 1280} / I_{G_{A_{1g}}}$ as a function of n , where $I_{1200 \times 1280}$ stands for the intensity of the 1200 and 1280 cm^{-1} A_{1g} bands with respect to their corresponding $G_{A_{1g}}$ band. a) Experimental [n]CPPs (lines are to guide the eye). Data from B3LYP/6-31G(d,p); b) twisted [n]CPPs; c) non-twisted [n]CPPs; d) non-twisted [n]LPPs; e) twisted [n]LPPs.

III.5 BLA and the Raman active A_{1g} modes. This section is aimed to address the Q/A character directly from the analysis of the changes in the bond distances as a new way to analyze the different BLA characteristics that occur in [n]CPPs and [n]LPPs. The conventional way to address the quinonoid/aromatic character connects that BLA values with the aromatic character if $BLA > 0$ and to the quinonoid character if it is < 0 . We also use this important indicator. In addition to the BLA value, we have additional data from the theoretical computations regarding the normal mode displacement vectors for each [n]CPP (one is illustrated in Fig. 11a) as well as their computed non-resonant Raman intensities. This provides an opportunity to compute an approximate amplitude mode displacement vector via eq. (5). We applied this formula to the non-twisted D_{nh} [n]CPPs which requires the summation over all the A_{1g} modes with significant intensity. We limited the summation to the following modes: $\sim 500\text{ cm}^{-1}$ [RFM], 800 cm^{-1} , $\sim 1200\text{ cm}^{-1}$, $\sim 1280\text{ cm}^{-1}$, $\sim 1580\text{ cm}^{-1}$ [$G_{A_{1g}}$ mode], and 3200 cm^{-1} (C-H A_{1g} mode). The displacement parameters for the resulting modes are depicted in Fig. 11b. Since displacement vectors are normalized, there are no absolute values associated with the BLA-like geometry change along the vibrational coordinate. For this reason, we use ratios of displacements and we compare those with the traditionally obtained geometry changes associated with BLA changes along the aromatic/quinonoid geometry changes.

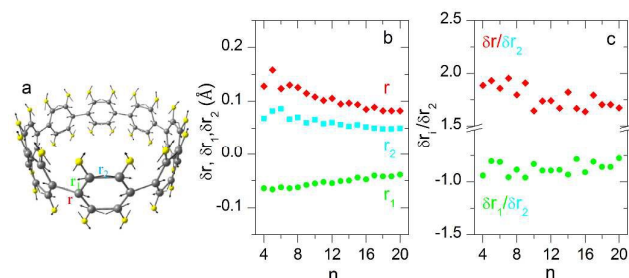


Figure 11. Normalized (\vec{B}_1) amplitude modes of [n]CPPs as evaluated by eq. (5). a) Displacement pattern for [8]CPP. b) Components of the amplitude mode in terms of δr , δr_1 and δr_2 as a function of n (the signs comply with the BLA pattern); c) BLA parameters defined in eq. (7), as a function of n , evaluated from the components shown in (b).

In Fig 1b the displacements involved in C-C stretching are characterized by the changes of the three parameters, as per Fig. 3a: δr , δr_1 and δr_2 . The signs are the same for δr , δr_1 and the opposite for δr_2 . In an attempt to compare them and being able to define the aromatic/quinonoid geometry change, in Fig 11c the ratios $\delta r/\delta r_2$ and $\delta r_1/\delta r_2$ are represented against n . It can be observed that the ratio $\delta r/\delta r_2$ is ~ 2 and its value becomes larger as n decreases. On the other hand, the ratio $\delta r_1/\delta r_2$ remains nearly constant at about -1.25 for any n . The positive $\delta r/\delta r_2$ and higher ratio for the smaller n CPPs clearly shows the strengthening of the C-C force constant along r , with the intensification of the quinonoid character as n decreases. Note that this trend is gradual, without showing a critical n value.

There is no requirement that the CC bond lengths added together along the carbon skeleton of [n]LPPs or [n]CPPs, (R , in eq. (6)) should be constant and thus we cannot assume that the BLA mode should obey approximately such a condition:

$$R = r + r_2 + r_1 + r'_1 = \text{constant} \quad (6)$$

However, this geometrical restriction on R does not apply for the \vec{B}_1 mode displacement vectors (accounted in δR) as shown in Fig. 11c for all n values. For further and unbiased characterization of the displacements, we define two relative displacement parameters:

$$\Delta = -\delta r/\delta r_1 \quad (7a)$$

$$\Delta_2 = -\delta r_2/\delta r_1 \quad (7b)$$

where δr , δr_1 , and δr_2 refer to the changes of the respective bond lengths. Large Δ indicates large change in r , large Δ_2 indicates large change in r_2 both compared to the changes in r_1 .

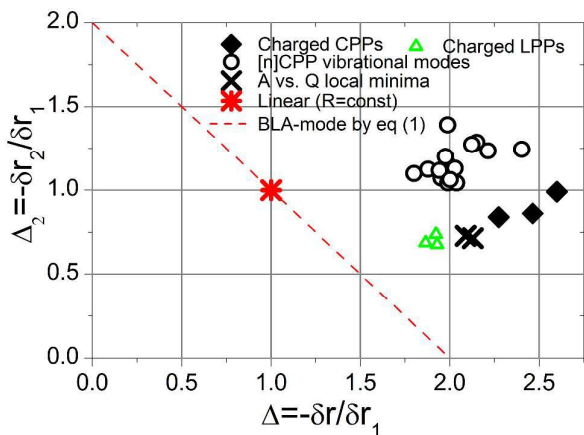


Figure 12. Variations of the relative values of Δ and Δ_2 displacement parameters. Black diamonds are values for the oxidized/reduced [n]CPPs and [n]LPPs; circles are values obtained from our analysis by eq. (5) of all [n]CPP discussed in this work. The red dashed line indicates no change in the overall sum along the conjugation path as per eq. (6). X refer to values for [n]CPP with $n=4$ and between their A and Q local minima on their respective PES (Scheme 2). Red star refers to the BLA mode that satisfies eq. (1a).

In Fig. 12, pairs of Δ and Δ_2 values from three different sources of changes in the BLA pattern are collected: (i) from the analysis of the geometry changes due to oxidation or reduction based on [5]CPP⁺, [5]CPP²⁺, [5]CPP²⁻, and [3], [4], [5]LPP²⁺, (ii) from the analysis of the BLA displacement vectors based on eq. (5) in the neutral [n]CPPs, and (iii) from the comparison of the A and Q structures in the valence tautomers of [n]CPP with $n=4$, and 5. We also show in Fig. 12 the geometry changes that are possible under the compliance with eq. (1a) and eq. (6).

To our surprise we find some variations, although not very large, of the BLA patterns (defined from displacement parameters) regarding the expected changes from the narrowly defined BLA mode of eq. (1a). Interestingly, the changes are classified by groups and are even more subtle from molecule to molecule. Overall for each of these three groups, the changes in r are about twice in magnitude compared with the changes in r_1 while changes in r_2 are comparable to changes in r_1 . These changes however are not evenly distributed among r , r_1 and r_2 . The important implication therefore is that the various structural modifications can be characterized and distinguished in terms of the qualitative aromatic (A) vs. quinonoid (Q) structural change using these new parameters ($\mathcal{C}_1 = \delta r/\delta r_1$ and $\mathcal{C}_2 = \delta r_2/\delta r_1$) which are sensitive to geometrical changes along the A to Q transition. This two dimensional characterization shows much more detail than the BLA change as defined in eq. (1a) and shown in Figs. 5a. Accordingly, the A vs. Q geometry change is dominated by the change of the inter-ring distance, δr which is approximately twice compared to δr_1 and δr_2 in the three discussed groups. For this reason one can identify a change of direction from an A to a Q structure even if such a quinonoid structure cannot be identified experimentally or theoretically as a local minimum for a given system.

Conclusions

In this paper, for the first time, a systematic study of the structural and electronic properties of the [n]CPP series in comparison with their linear analogues, oligoparaphenylenes, is conducted. Particular emphasis is put on the structural differences and in their different behavior as a function of the molecular size from Raman spectroscopy and DFT computations. Benzene ring bending angles, inter-rings torsions, BLA patterns and HOMO-LUMO gaps are carefully compared for both series. The distinctive evolution of these structural parameters indicates the presence of a particular type of π -electron delocalization associated with the cyclic geometry which is absent in the linear congeners, or cyclic π -conjugation. Cyclic π -conjugation is manifested by the large benzene ring bendings, minimal inter-ring torsions and small HOMO-LUMO gaps. In contrast, linear π -conjugation produces no phenyl deformation, minimal inter-ring torsion and slightly reduced HOMO-LUMO gaps. The strong difference that activates cyclic π -conjugation is the partial rupture of benzene aromaticity that liberates electrons from the ring confinement towards a more quinonoid configuration and facilitates cyclic delocalization. In contrast, aromaticity in [n]LPPs mostly inhibits linear π -conjugation. Compared with [n]LPPs, we find several Raman spectroscopic marks directly attributed to cyclic π -conjugation such as larger intensity distribution along all the A_{1g} modes, not only the $G_{A_{1g}}$ as in [n]LPPs and larger frequency shifts with size for the detected Raman bands. We have found that a generalized definition of BLA in terms of displacement parameters provides more insights into this particular aromatic-quinonoid balance in the cyclic π -structures. A way of obtaining such displacement parameters is obtained from the ECC mode vibrational eigenvectors extracted from the vibrational analysis associated with the most intense bands of the Raman spectra.

We also conclude that the concept of a quinonoid-like structure is not limited to situations where such a tautomeric structure can be computationally identified as a local minimum. Quinonoid structures provide useful tools for the analysis of structural changes upon Raman active vibrations even if such a quinonoid structure is not present as a local minimum.

In summary, an exhaustive analysis of the differences and similarities between [n]LPPs and [n]CPPs is carried out revealing different aromatic/quinonoid characters of the benzene rings. At the end, we extract clear differences between linear π -conjugation and cyclic π -conjugation.

Acknowledgements:

The authors acknowledge Paula Mayorga-Burrezo for her help during the Raman measurements. Financial support from the Spanish Ministry of Economy (CTQ2012-38599-C02-02, CTQ2012-33733), Junta de Andalucía (Project P09-FQM-4708) and Comunidad de Madrid (S2009/PPQ-1551) are acknowledged. M.P.A. is grateful to the Spanish MEC for an FPU grant and a Visiting Scientist Fellowship to Georgetown University. M.C.R.D. thanks the MICINN for a Ramón y Cajal Research contract. We thank the U. S. National Science Foundation for its support of this research at Georgetown University (grant number CHE-1006702).

References

- 1 H. Omachi, T. Nakayama, E. Takahashi, Y. Segawa and K. Itami, *Nature Chem.*, 2013, **5**, 572-576.
- 2 R. Jasti, J. Bhattacharjee, J. B. Neaton and C. R. Bertozzi, *J. Am. Chem. Soc.*, 2008, **130**, 17646-17647.
- 3 T. Sisto, M. R. Golder, E. S. Hirst and R. Jasti, *J. Am. Chem. Soc.*, 2011, **133**, 15800-15802.
- 4 P. J. Evans, E. R. Darzi and R. Jasti, *Nature Chem.*, 2014, **6**, 404-408.
- 5 J. Xia and R. Jasti, *Angew. Chem. Int. Ed.*, 2012, **51**, 2474-2476.
- 6 M. Fujitsuka, C. Lu, T. Iwamoto, E. Kayahara, S. Yamago and T. Majima, *J. Phys. Chem. A*, 2014, **118**, 4527-4532.
- 7 S. E. Lewis, *Chem. Soc. Rev.* 2015, **44**, 2221-2304.
- 8 H. Chen, M. R. Golder, F. Wang, S. K. Doorn, R. Jasti, S. Tretiak and A. K. Swan, *J. Phys. Chem. C*, 2015, **119**, 2879-2887.
- 9 H. Chen, M. R. Golder, F. Wang, R. Jasti and A. K. Swan, *Carbon*, 2014, **67**, 203-213.
- 10 N. Toriumi, A. Muranaka, E. Kayahara, S. Yamago and M. Uchiyama, *J. Am. Chem. Soc.*, 2015, **137**, 82-85.
- 11 B. M. Wong, *J. Phys. Chem. C*, 2009, **113**, 21921-21927.
- 12 (a) Y. Segawa, A. Fukazawa, S. Matsuura, H. Omachi, S. Yamaguchi, S. Irle and K. Itami, *Org. Biomol. Chem.*, 2012, **10**, 5979-5984. (b) Y. Segawa, H. Omachi and K. Itami, *Org. Lett.*, 2010, **12**, 2262-2265.
- 13 S. Yamago, E. Kayahara, T. Iwamoto, *Chem. Rec.* 2014, **14**, 84-100.
- 14 T. Iwamoto, Y. Watanabe, T. Sadahiro, T. Haino and S. Yamago, *Angew. Chem. Int. Ed.*, 2011, **50**, 8342-8344.
- 15 M. R. Golder, B. M. Wong and R. Jasti, *Chem. Sci.*, 2013, **4**, 4285-4291.
- 16 E. Kayahara, T. Kouyama, T. Kato, H. Takaya, N. Yasuda and S. Yamago, *Angew. Chem. Int. Ed.*, 2013, **52**, 13722-13726.
- 17 E. H. Házó, J. G. Duque, X. Tu, M. Zheng, A. R. H. Walker, R. H. Haige, S. K. Doorn and J. Kono, *Nanoscale*, 2013, **4**, 1411-1439.
- 18 F. Sibbel, K. Matsui, Y. Segawa, A. Studer and K. Itami, *Chem. Commun.*, 2014, **50**, 954-956.
- 19 S. Yamago, Y. Watanabe and T. Iwamoto, *Angew. Chem. Int. Ed.*, 2010, **49**, 757-759.
- 20 Y. Segawa, P. Šenel, S. Matsuura, H. Omachi and K. Itami, *Chem. Lett.*, 2011, **40**, 423-425.
- 21 E. Kayahara, Y. Sakamoto, T. Suzuki and S. Yamago, *Org. Lett.*, 2012, **14**, 3247-3247.
- 22 J. Xia, J. W. Bacon and R. Jasti, *Chem. Sci.*, 2012, **3**, 3018-3021.
- 23 Y. Segawa, S. Miyamoto, H. Omachi, S. Matsuura, P. Senel, T. Sasamori, N. Tokitoh and K. Itami, *Chem. Int. Ed.*, 2011, **50**, 3244-3248.

- ²⁴ M. Peña-Alvarez, P. M. Burrezo; M. Kertesz, T. Iwamoto, S. Yamago, J. Xia, R. Jasti, López J. T. Navarrete, M. Taravillo, V. G. Baonza and J. Casado, *Angew. Chem. Int. Ed.* **2014**, *53*, 7033-7037.
- ²⁵ E. R. Darzi, R. Jasti, *Chem. Soc. Rev.*, 2015, **44**, 6401-6410.
- ²⁶ S. M. Bachrach and D. Stück, *J. Org. Chem.*, 2010, **75**, 6595-6604.
- ²⁷ M. Banerjee, R. Shukla and R. Rathore, *J. Am. Chem. Soc.*, 2009, **131**, 1780-1786.
- ²⁸ a) P. A. Irvine, D. C. Wu and P. J. Flory, *J. Chem. Soc., Faraday Trans. 1*, 1984, **80**, 1795-1806. (b) K. N. Baker, A. V. Frai, T. Resch, H. C. Knachel, W. W. Adams, E. P. Socci and B. L. Farmer, *Polymer*, 1993, **34**, 1571-1587. c) M. Rinke, H. Gusten and H. J. Ache, *J. Phys. Chem.*, 1986, **90**, 2666-2669.
- ²⁹ (a) J. L. Bredas, R. R. Chance and R. Silbey, *Phys. Rev. B*, 1982, **26**, 5843-5854 (b) T. A. Skotheim, *Handbook of Conducting Polymers*, Ed.; Dekker: New York, 1986; Vols. 1 and 2. (c) J. L. Bredas, R. R. Chance, *Conjugated Polymeric Materials*; Eds.; Kluwer Academic: Dordrecht, 1990. (d) Y. S. Lee, M. Kertesz, R. L. Elsenbaumer, *Chem. Mater.* 1990, **2**, 526-530.
- ³⁰ (a) B. Horowitz, *Solid State Commun. Colloq.* 1982, **42**, 729; (b) B. Horowitz *Phys. Rev. B*, 1987, 1535.
- ³¹ G. Zerbi, M. Gussoni and C. Castiglioni, (J. L. Bredas and J. Silbey, Eds.) Kluwer, New York, 1991, p. 435.
- ³² M. G. Gussoni, W. B. Person,; G. Zerbi, *Vibrational Intensities in Infrared and Raman Spectroscopy*; G. Eds. Elsevier: Amsterdam, 1982, 221-238.
- ³³ L. Cuff, C. Cui and M. Kertesz, *J. Am. Chem. Soc.* 1994, **116**, 9269-9274.
- ³⁴ A. Marucci, M. A. Pimenta, S. D. M. Brown, M. J. Matthews, M. S. Dresselhaus and M. Endo, *J. Mater. Res.*, 1999, **14**, 3447-3454.
- ³⁵ M. Kertesz, C.H. Choi and S. Yang, *J. Chem. Rev.*, 2005, **105**, 3448 - 3481
- ³⁶ T. Iwamoto, Y. Watanabe, Y. Sakamoto, T. Suzuki and S. Yamago, *J. Am. Chem. Soc.*, 2011, **133**, 8354-8361.
- ³⁷ A. P. Rice, F. S. Tham and E. L. Chronister, *J. Chem. Cryst.*, 2013, **43**, 14-25.
- ³⁸ Y. Delugeard, J. Desuiche and J. L. Baudour, *Acta Cryst.*, 1976, **B32**, 702-705.
- ³⁹ J. L. Baudour, *Acta Cryst.* 1991, **B47**, 935-949
- ⁴⁰ H. Kuzmany, A. Imhoff, D. B. Fitch and A. Sarhangi. *Phys. Rev. B.*, 1982, **26**, 7109-7112.
- ⁴¹ http://www.gaussian.com/g_tech/g_ur/k_scan.htm
- ⁴² G. Heimel, D. Somitsch, P. Knoll, J.L. Bredas and E. Zojer, *J. Chem. Phys.*, 2005, **122**, 114511-114519.
- ⁴³ V. Hernandez, C. Castiglioni, M. Del Zoppo and G. Zerbi, *Phys. Rev. B.*, 1994, **50**, 9815-9823.
- ⁴⁴ N.I Nijegorodov, S. W. Downey and M. B. Danailov, *Spectrochim. Acta A.*, 2000, **56**, 783-795.
- ⁴⁵ C. X. Cui, M. Kertesz and Y. Jiang, *J. Phys. Chem.*, 1990, **94**, 5172-5179.
- ⁴⁶ L. W. Shacklette, H. Eckhardt, R. R. Chance, G. G. Miller, D. M. Ivory and R. H. Baughman, *J. Chem. Phys.*, 1980, **73**, 4098-4120.
- ⁴⁷ G. Zannoni and G. Zerbi, *J. Chem. Phys.*, 1985, **82**, 31- 38.
- ⁴⁸ G. Zerbi, B. Chierichetti and O. Inganas, *J. Chem. Phys.*, 1991, **94**, 4637-4645.
- ⁴⁹ G. P. Brivio, E. Mulazzi, *Phys. Rev. B.* 1984, **30**, 876-882.
- ⁵⁰ H. Ohtsuka, Y. Furukawa, M. Tasumi, *Spectrochim. Acta. Part A*, 1993, **49**, 731-737.
- ⁵¹ Y. Pelous, G. Froyer, C. Herold, S. Lefrant, *S. Synth Met.* 1989, **29**, E17.
- ⁵² L. Adamska, I. Nayyar, H. Chen, A. K. Swan, N. Oldani, S. Fernandez-Alberti, M. R. Golder, R. Jasti, S. K. Doorn, S. Tretiak, *Nano Lett.*, 2014, **14**, 6539-6546.